

The Soft X-ray Spectrum of Scattering–Dominated AGN

Hagai Netzer ¹, T.J.,Turner ^{2,3}, I.M.,George ^{2,3}

ABSTRACT

This paper discusses the properties of scattering–dominated active galactic nuclei (AGN). We define these to be AGN for which the direct line-of-sight to the continuum source is obscured by Compton-thick material. The aim is to construct, for the first time, a model consistent with X-ray line luminosities, line ratios and various luminosity indicators. The *ASCA* spectra of six such sources show several X-ray lines that can be reliably measured, mostly due to highly ionized magnesium, silicon sulphur and iron. These enable us to investigate the physical conditions of the scattering material. The sources show evidence of He-like and H-like iron lines that are likely to be produced in hot ($T \sim 10^6$ K) photoionized gas. By measuring the EW of the lines, and by constructing a diagnostic line-ratio diagram, we demonstrate that the silicon and magnesium lines are produced by the same gas emitting the highly ionized iron lines. The properties of this gas are rather different from the properties of warm absorbers in type I AGN. Neutral 6.4 keV iron lines are also detected, originating in a different component which can be either Compton-thin or Compton-thick. The best measured iron lines suggest an enhancement of $n_{\text{Fe}}/n_{\text{H}}$ by a factor ~ 2 compared to solar, in both the hot and cool Compton-thin components. We further show that in four of the sources, the Fe $K\alpha$ (6.4 keV)/ $H\beta$ ($\lambda 4861\text{\AA}$) line ratio is consistent with that predicted for typical narrow line region clouds, and the reddening corrected $H\beta$ is known, provided the column density is larger than $\sim 10^{22.5} \text{ cm}^{-2}$, α_{ox} is smaller than 1.3. For some sources, this is a viable alternative to the commonly assumed Compton thick medium as the origin of the 6.4 keV iron line.

Subject headings: galaxies:abundances - galaxies:Seyfert - galaxies:active - line:formation - X-ray:galaxies

¹School of Physics and Astronomy and the Wise Observatory, The Raymond and Beverly Sackler Faculty of Exact Sciences, Tel-Aviv University, Tel-Aviv 69978, Israel

²Laboratory for High Energy Astrophysics, Code 660, NASA/Goddard Space Flight Center, Greenbelt, MD 20771

³University Space Research Association

1. Introduction: Scattering–Dominated AGN

The optical and X-ray properties of type II AGN (i.e. those showing prominent narrow emission lines and very faint, if any, broad lines) have been discussed in numerous recent papers that contain the analysis of their morphology, spectrum, geometry and relationship to type I (broad emission line) AGN. Various names, including Seyfert 2, narrow emission line galaxies (NELG), and narrow line X-ray galaxies (NLXGs) have been used to describe these objects. Obviously, there is some subjectivity in the classification of type II AGN leading to the assignment of a more than one “type” for some objects which have been studied by several authors. The geometry of the innermost region of such sources is a fundamental, yet still an open issue and the reader is referred to Antonucci (1993), and Mulchaey *et al.* (1994) for discussion and references regarding these questions.

X-ray observations offer a unique view of type II AGN, since X-rays can penetrate large column densities. This has been a subject of much research, for example, see recent papers by Turner *et al.* (1997a,b,1998). These authors found some surprising similarities between the X-ray spectra of type I and type II AGN. In some type II sources, the equivalent width (EW) of the 6.4 keV line is similar to that observed in Seyfert 1s and the line profiles show broad, redshifted wings. In other type II sources, like NGC 1068, EW(Fe K α) is an order of magnitude larger than in type I AGN, suggesting that the line is seen against a reduced continuum, presumably due to obscuration. Evidently, type II AGN fall into at least two X-ray categories; those where the central source is directly observed below 10 keV, and those where it is not. Hereafter we refer to those type II AGN whose 0.5–10 keV spectra are dominated by scattered radiation, “scattering–dominated AGN”, and they are the subject of this paper. We expect a good, but not necessarily a one-to-one correlation between such objects and those type II AGN who show highly polarized continuum and broad optical/UV emission lines, due to scattering (e.g. Tran 1995).

This paper investigates the properties of scattering–dominated AGN through detailed analysis of their 0.5–10 keV spectrum. We address the nature of the scattering medium and try to deduce its level of ionization, column density and covering fraction. We also investigate the metallicity of the gas and compare its properties to the ionized gas in Seyfert 1 galaxies, and to the narrow line region (NLR) gas. The analysis is aimed at a small number of scattering–dominated AGN whose *ASCA* spectra are of a sufficiently high quality to enable the measurement of at least 3 X-ray emission lines. It also suggests several new avenues for future study of such sources in preparation for the coming *AXAF* and *XMM* missions. In §2 we discuss the predicted spectra of such sources. In §3 we compare predictions to a detailed analysis of the *ASCA* spectra of six such galaxies. In §4 we discuss several implications of such a comparison, and implications for the state and the location of

the scattering medium and its composition.

2. The X-ray spectra of scattering-dominated AGN

In this section we show new calculations pertaining to scattering-dominated AGN. The calculations assume a simple geometry of a point-like source of X-ray and UV radiation surrounded by gas clouds of various locations, density and column density. The gas is photoionized by the radiation of the central source and no other excitation is assumed. The geometry is such that the line-of-sight to the central source is completely covered by a column density of 10^{24} cm $^{-2}$ or larger but the scattering medium has a clear view of the center and we have a clear view of the scattering gas. The parameters of the model are the gas covering factor, $C_f = \Omega/4\pi$, where Ω is the solid angle subtended at central source, density n_H , column density N_H , and the gas location. We shall make extensive use of the “X-ray Ionization Parameter”, $U_x = Q_{0.1-10 \text{ keV}}/n_H c$ (Netzer 1996), where $Q_{0.1-10 \text{ keV}}$ is the incident photon flux in the 0.1–10 keV band. This parameter is closely related to the ionization level of most observed highly ionized species. Conversion factors between U_x and the $U_{13.6 \text{ eV}}$ ionization parameter (defined over the entire Lyman continuum), are given in George *et al.* (1998).

The scattering gas is assumed to be distributed in a shell geometry and is made of a large number of small clouds with dimensions similar to the shell thickness. The shell is not complete since the obscurer (possibly a torus?) subtends a non-negligible solid angle as viewed from the center. For simplicity, we assume that U_x and N_H are the same for all clouds. All scattering and emission processes are assumed to be isotropic and the photons emitted from the cloud and reaching the observer are both those which ‘leak’ between the clouds and those transmitted through the clouds. For a uniform distribution of small clouds, the relative fraction of the two (i.e. the leaking photons and the attenuated ones) is uniquely specified by the covering factor C_f . The real situation can be rather more complex. For example, a geometry of $C_f < 1$ may involve extra absorption of *all* emitted photons. This can happen if a single large cloud is situated just outside the main scattering region, on the line of sight. In such a case, all emitted and scattered photons suffer extra attenuation on the way out. The present calculations do not include such complications.

The calculations presented here were performed using the photoionization code ION97. This code includes a full treatment of all important IR, optical, UV and X-ray transitions and solves, simultaneously, for the level of ionization, temperature and opacity of the exposed gas. For a full description and more references see Netzer (1996). The calculations assume two “canonical” spectral energy distributions (SEDs). We describe those either by

the energy slope α , i.e. where the luminosity, L_E , is related to the energy, E , as ($L_E \propto E^{-\alpha}$) or the photon slope where the number of photons, N , at energy E is given by Γ ($N_E \propto E^{-\Gamma}$). The first has a UV bump centered at 40 eV, a soft ($E > 100$ eV) X-ray component of $\alpha = 2$ changing gradually to a hard X-ray slope of $\alpha = 0.9$. The ratio of the two continuum components at 1 keV is soft(X-ray)/hard(X-ray)=0.5. For this SED, $\alpha_{ox}=1.38$. The second SED has a similar UV bump but a much flatter hard X-ray slope of $\alpha = 0.5$. In this case $\alpha_{ox}=1.13$, typical of low luminosity Seyfert 1 galaxies. The fiducial gas density is $n_H = 10^8 \text{ cm}^{-3}$ which adequately represents the physical conditions over the density range of 10^5 to 10^{11} cm^{-3} . Unless otherwise specified, the following standard metallicity (which is similar to solar metallicity) is assumed throughout:

H:He:C:N:O:Ne:Mg:Si:S:Ar:Fe= $10^4:1000:3.7:1.1:8:1.1:0.37:0.35:0.16:0.037:0.4$.

The more important ingredients of the model are the ionization parameter U_x , which determines the level of ionization and line intensity, the column density N_H , which determines the fraction of the incident radiation absorbed by individual clouds, and a parameter which we name “reprocessing factor”, $R_f(E)$. This energy-dependent parameter, represents the fraction of the radiation of the central source reaching the observer via scattering. For small N_H and small C_f , it is almost energy independent and is given by $R_f \simeq \tau_e C_f$, where τ_e is the Compton optical depth of the clouds.

Our aim in this work is to investigate the parameter space occupied by scattering-dominated AGN. Thus, the observed continuum must be consistent with the assumed intrinsic SED, the observed line ratios must correctly reflect the various neutral and ionized components, and R_f must be consistent with the bolometric luminosity of the source. Previous studies have only considered a sub-set of these variables. Here we consider them all self-consistently for the first time. Below we discuss the predicted X-ray lines and scattered continuum.

2.1. X-ray emission lines

2.1.1. The iron K lines

The absorption of the hard X-rays by iron ions results in Fe $K\alpha$ line emission due to fluorescence (all ions up to FeXXIV), resonance line absorption (ions with ten or fewer electrons) and recombination. Fe $K\beta$ transitions, with about 10 percent the intensity of the corresponding Fe $K\alpha$ lines, are also emitted. These processes have been discussed, extensively, in the literature and will not be reviewed here. The reader is referred to Kallman and Krolik (1987), George and Fabian (1991) and Leahy and Creighton (1993)

for calculations of the Fe $K\alpha$ lines in neutral gases, and to Matt (1994) and Matt, Brandt & Fabian (1996), for cases involving ionized material. ION97 includes all such processes and the lines are calculated under the assumption of complete isotropy of the scattered radiation. This simplified assumption can introduce small differences compared with the full, angle dependent calculations (e.g. Matt *et al.* 1996, Fig. 5). However, the geometry under consideration is sufficiently complex, and most likely involves a combination of various angles, that we see no reason to consider this additional complication.

The observed EWs depend on the level of ionization, the column density, the gas expansion or microturbulent motion (which determine the resonance line optical depth), the incident continuum shape and the iron abundance. Unless otherwise specified, all calculations assume microturbulent motion with a line width fixed at the local sound speed, i.e. similar to the hydrogen thermal width. The calculations are restricted to $\tau_e < 1$ since the present transfer approximation is not adequate for Compton-thick material.

Fig. 1 shows calculated EW($K\alpha$) for “neutral” (FeI–XVI) and He-like (FeXXV) iron lines, over a range of ionization parameter and column density. It demonstrates that for large N_H , the maximum EW of the two is comparable. The reason is that both the scattered continuum and the $E > 7.1$ keV flux are proportional to the column density of the ionized gas, and the absorption cross sections of the different iron ions are very similar. (The neutral lines can absorb slightly more photons but the recombination efficiency of the FeXXV line is larger than the fluorescence yield of the low ionization ions which compensates for this). This is not the case for small N_H , where EW(FeXXV) is considerably larger due to resonance absorption of continuum photons by the 6.7 keV lines. As to the dependence on C_f , see below.

Fig. 2 shows a detailed dependence of the various $K\alpha$ intensities on U_x , for the specific column density of $10^{22.4}$ cm^{-2} and $C_f = 0.5$. The equivalent widths shown are measured with respect to the *scattered continuum* and are designated EW(gas).

As seen from the diagram, *the summed* EW($K\alpha$) is almost independent of U_x , demonstrating that for the assumed gas motion, with the sound-speed line width, resonance absorption is not very important compared with continuum (otherwise the EWs of the iron lines where this process can take place, would be much larger). The reason is the large optical depth in all resonance transitions. For example, the optical depth of the FeXXV 6.7 keV line for this N_H and for $U_x = 10$ is about 9, i.e. resonance absorption is efficient only for turbulent motion exceeding about 1000 km/sec.

2.1.2. The soft X-ray lines

We define these transitions to include all lines with $0.5 < E < 6.4$ eV. The strongest are He-like and H-like lines of the most abundant elements. Under the conditions assumed here, most of the emitted flux is due to recombination and resonance absorption is of little significance. Auger excited $K\alpha$ transitions in ions with more than three electrons can be important too, despite the very small fluorescence yield, because of the larger photon flux at low energies (Netzer and Turner 1997). Collisionally dominated lines are usually very weak, because of the low temperature of the photoionized gas. This is also true for the collisionally-excited Fe L-shell lines. However, the recombination lines due to Fe L-shell transitions do make significant contributions to the observed flux around 0.8–1.2 keV. For the treatment of those lines see Netzer (1996).

Fig. 2 shows also the calculated $EW(\text{gas})$, as a function of U_x , for several soft X-ray lines. Fig. 3 shows the relative line intensities obtained by normalizing the line flux to the *incident* continuum at a specific energy (0.65 keV). This diagram illustrates the processing efficiency of the various lines. Fig. 4 gives yet another view of the information presented in Fig. 2, this time over a large range in column density and ionization parameter.

While most EWs are not sensitive to the exact value of the covering fraction, this is not the case when C_f approaches unity. This can be explained by noting that for optically thin gas, the relative line to scattered continuum flux is independent of the covering fraction. This is also the case for large optical depth and $C_f < 0.9$, since the line and adjacent continuum photons undergo similar amount of absorption and much of the observed flux is due to leakage through “holes” in the cloud configuration. However, for large optical depth and covering fraction approaching unity, much of the line and continuum radiation gets absorbed on the way out. Minor differences in the optical depth structure can result in large changes in equivalent width. The same is true for situations where the 4π covering fraction is much less than unity but the emitted photons pass, on the way out, through gas with substantial optical depth. Such situations must be treated with care and are not considered here. Needless to say, the absolute line flux is very sensitive to the value of C_f and obtains its maximum value at $C_f \sim 0.6 - 0.8$ (Netzer 1996).

2.2. The scattered continuum

The SED of the scattered continuum is another indicator of the ionization state and column density of the gas. This has been discussed in numerous papers since the first work of Lightman and White (1988) and many examples are shown in Netzer (1993), Netzer,

Turner and George (1994), Zycki and Czerny (1994), Zycki *et al.* (1994) and Ghisellini, Haardt and Matt (1994).

The 0.5–10 keV continuum of several scattering-dominated AGN (see §3) are considerably flatter than typical, type-I AGN continua. We assign this to the unique characteristic of scattered SEDs. To illustrate this point, and to enable a meaningful comparison with the emission line spectrum (§4), we show, in Fig. 5, two calculations of scattered spectra, using our canonical $L_E \propto E^{-0.9}$ continuum. One has a column density of 10^{23}cm^{-2} and very low ionization ($U_X=10^{-3}$) and the other a column of 10^{22}cm^{-2} and a much higher ionization ($U_X=10$). The two have the same covering factor and are combined in such a way that the relative intensity of the neutral and highly ionized $K\alpha$ lines are similar to what is observed in three of the sources under discussion (§3). As evident from the diagram, large-column, low-ionization gas results in a rising SED while the slope of the highly ionized gas resembles the incident continuum. The combination of the two in the right proportions can produce very flat continua, as observed in several scattering-dominated AGN.

Calculations such as the ones shown here can be used to compare the observed continuum shape with the relative emission line strength. In particular, the analysis of the Fe $K\alpha$ blend is most useful since, for a typical type-I AGN SED, the transition to He-like and H-like iron occurs at $U_X \simeq \text{few}$ (Fig. 2). The relative strengths of such lines must therefore tell us the relative proportion of the various scattered continuum components. Finally, the observed continuum luminosity is related to the intrinsic SED through the reprocessing factor R_f . As shown by Turner *et al.* (1997b), and explained in detail below, this parameter can be inferred from a comparison of the X-ray luminosity with luminosity indicators at other wavelengths.

3. Comparison with *ASCA* observations

We have chosen to analyze six narrow line Seyfert galaxies with the most prominent EW(Fe $K\alpha$) available in the *ASCA* archives (as of June 1997): Mrk 3, NGC 6240, NGC 1068, Circinus A, Mrk 348 and NGC 4388. These sources are thus likely to be scattering-dominated AGN. Three of the sources (Mrk 3, NGC 6240, NGC 1068) are from the Turner *et al.* (1997a) sample, and the results from Circinus A have been previously presented by Matt *et al.* (1996). NGC 1068 has also recently been discussed by Netzer and Turner (1997) and we use the line measurement given in that paper. For the others, we have remeasured all prominent X-ray lines, by criteria explained below, and some of our results are therefore different from those listed in the original references. Other suspected

objects of this type (Turner *et al.* 1997b) have spectra with much lower S/N and are not suitable for this kind of detailed analysis.

The sources presented here were systematically analyzed using the same method as described in Turner *et al.* (1997a). We do not use data below 0.6 keV in the spectral fitting because of some uncertainty in the *ASCA* XRT/SIS calibration, rendering those data points artificially low. Data from both pairs of SIS and GIS instruments were analyzed simultaneously, but with the normalization of each dataset allowed to vary relative to the others (to allow for small uncertainties in the relative flux calibrations of the detectors and the different extraction cells employed). All fluxes, luminosities and normalizations are tabulated for SIS0 (with no correction for the point-spread function, or counts lost off the edge of the chip, both are small effects in these cases). We utilized the gain-corrected pulse-invariant (PI) channels for all instrument datasets, and the spectra were binned for the spectral analysis such that each channel contained at least 20 counts allowing χ^2 minimization techniques. Response matrices released on 1994 Nov 9 and 1995 March 6 were used for the SIS and GIS data respectively, and the spectral analysis performed using XSPEC (v10.0).

We employ simple models to try to achieve an acceptable parameterization of the X-ray continuum shape for each dataset. The purpose is to allow accurate line measurement and we attach no physical significance to the assumed continuum components. To do this we first fit the 0.6–10 keV data excluding the 5–7 keV band which is dominated by iron K-shell line photons. We considered a number of continuum models in turn, finding that a double power-law model provided a satisfactory parameterization of each source. The absorption of the soft X-ray power-law column was constrained to be greater than or equal to the Galactic line-of-sight column (hereafter denoted N_{Hgal}), while the absorption of the hard power-law was independent of this, and unconstrained. Fig. 6 shows the SIS data and fitted models to the six datasets. Many X-ray emission lines are evident in these datasets. The 5–7 keV data were returned to the fit, and gaussian model components were added to the model until we had tested for the presence of all expected lines.

Line widths were constrained to be narrow (< 3 eV), and we took the approach of adding numerous narrow components to the model, even when too closely spaced to be resolved by *ASCA* with the intent that we model all the line flux in the data. However, we tabulate only the resolvable quantities, i.e. we note the sum of FeX–XXIV, FeXXV–XXVI+ Fe K β , SiXII–XIII and SiXIV–XV. The SiXIV 2.0 keV line is currently problematic for *ASCA*, as it is at an energy close to where most of the calibration ‘adjustments’ have been made. Bearing this in mind, the strength of this line is currently subject to additional unquantifiable uncertainty, in excess of the statistical error tabulated.

As this analysis also revealed evidence for some broad unmodeled residuals in the Fe $K\alpha$ regime, we allowed a broad Fe $K\alpha$ component, which may physically represent either the Compton scattered wing or, more likely (Turner *et al.* 1998), the asymmetric component from the putative accretion disk. Furthermore, we assumed that scattering-dominated AGN have an intrinsic broad Fe $K\alpha$ line component of the same strength and shape as that observed in Seyfert 1 galaxies (Nandra *et al.* 1997, Turner *et al.* 1998). This line is scattered, like the 6.4 keV continuum, by the surrounding gas and ought to be included in the fit. This component was constrained to be ≤ 300 eV, relative to the hard X-ray continuum, to keep it within the range of strengths observed for Seyfert 1 galaxies. Its inclusion generally improved the fit significantly, thus the list in Table 1 takes the broad component into account, even though it is not tabulated.

Our continuum fitting procedure includes two power-law components, specified by the photon slope Γ , and one or two absorbers. The first absorber is the deduced galactic column. The second is required for NGC 6240 and Mkn 348, where we detect the direct component at high energies. As already mentioned, the only purpose is to get a reasonable fit to allow accurate line measurements and reliable estimates of the 2–10 keV luminosities (attenuation was taken into account when estimating the intrinsic luminosities). The parameters are listed in Table 2 and the ones required for NGC 1068 are given in Netzer and Turner (1997) (for this source $L_{2-10} = 1.8 \times 10^{41} \text{erg s}^{-1}$).

4. Discussion

The following analysis is based on the line fluxes listed in Table 1 as well as on the analysis of the *ASCA* spectrum of NGC 1068 (Netzer and Turner, 1997, Table 1). Obviously, the number of objects, and the number of measurable lines per object, are very small and the information content regarding the group properties is rather limited.

The most severe complication in analyzing the *ASCA* spectra is the likely contamination of the nuclear spectrum by extended, non-nuclear emission. This may be the result of hot gas in star forming regions, supernova remnants, or any other gas at $T \simeq 10^7$ K. The limited *ASCA* spatial resolution (with a half-power diameter ~ 3 arcmin), combined with the relative weakness of the scattered X-ray continuum, makes it almost impossible to separate the photoionized gas and hot plasma contributions. Indeed, some sources (e.g. NGC 1068) show clear indication of extended X-ray emission which is most likely due to starburst activity. This issue will not be resolved before *AXAF* observations (with a half-power diameter < 1 arcsec). Below we comment on the information obtained from the study of the Fe $K\alpha$ complex and address the potential use of diagnostic diagrams in the analysis of the

spectrum of scattering-dominated AGN.

4.1. The $K\alpha$ complex and the iron abundance

Except for NGC 1068, all our measurements of the 6–7 keV complex are somewhat ambiguous since we can not reliably resolve the highly ionized (6.7 and 6.96 keV) Fe $K\alpha$ lines from the neutral $K\beta$ (~ 7.1 keV) line. Therefore, the analysis of the high ionization lines pertains to the *combined intensity* of the H-like and He-like iron lines, which was obtained by subtracting the expected $K\beta$ flux (10% the flux of the 6.4 keV $K\alpha$ line) from the total. This makes the combined FeXXV-XXVI line intensity in NGC 3488 consistent with zero because of the uncertainty on the $K\beta$ flux (see Table 1) and the ones in Mkn 348 consistent with zero because of the large intrinsic error. The uncertainty in the relative strength of the 6.4 and 6.9 keV component is also affected by the uncertainty in the assumed, scattered broad 6.4 keV line.

The galaxies with measurable soft X-ray lines represent two different groups. In one object (NGC 1068), the highly ionized iron lines are comparable in strength to the 6.4 keV line. In three others (Circinus, Mkn 3 and NGC 4388) the combined intensity of the He-like and H-like iron lines is only about 10-15% the intensity of the low ionization component. Mkn 348 is possibly an intermediate case but the observational uncertainties are too large to tell. The intensity of the high ionization iron lines in NGC 6240 is unknown, because of their proximity to the strong 7.1 keV absorption feature due to 2×10^{24} cm⁻² of neutral absorber. However, a comparison of the 6.4 keV intensity with the soft X-ray lines suggests that this source belongs to the same group as Mkn 3 and Circinus. As for the lines of silicon, magnesium and sulphur, there are only three sources where reliable line ratios can be obtained and they all look quite similar (see below).

Regarding the 6.4 keV iron line, a comparison of the measured line intensities with the calculations shown in Figs. 2 and 3, indicate that in all sources where this line is much stronger than the 6.7–7.0 keV complex, the line can not originate in the same component producing the strong magnesium, silicon and sulphur lines. We therefore suggest that in those sources, much of the 6.4 keV line emissivity is due to reprocessing in a large column of low-ionization gas. As for NGC 1068, the 6.4 keV line in this source may be due to warm ($T_e \simeq 2 \times 10^5$ K) photoionized gas (Marshall *et al.* 1993; Netzer & Turner 1997). This idea is in conflict with the Iwasawa *et al.* (1997) model (see below). We conclude that in four (perhaps five) of the six sources, the reprocessing efficiency (R_f) of the neutral component is much greater (a factor of 5–10) than that of the ionized component.

Given the level of ionization of the gas producing the 6.4 keV iron line, and the shape of the ionizing continuum, we can estimate the iron abundance from the observed EW(Fe K α) in two interesting limits. The first corresponds to Compton–thin gas and has been discussed by Krolik and Kallman (1987), Matt *et al.* (1996) and others. In this case, assuming negligible resonance line absorption and complete isotropy of the scattered continuum radiation (as appropriate for a case where the scattering medium is viewed at all possible angles),

$$\text{EW}(6.4 \text{ keV}) \simeq 3.17 \left[\frac{1.11^{1-\Gamma}}{2 + \Gamma} \right] \left[\frac{F_Y}{0.3} \right] \left[\frac{n_{\text{Fe}}/n_{\text{H}}}{4 \times 10^{-5}} \right] \text{ keV} , \quad (1)$$

where F_Y is the fluorescence yield (of the order of 0.3 for low ionization iron). In deriving this expression we have adopted the small column density limit which allows us to neglect the absorption of the emitted K α photons on the way out. A much slower (logarithmic) dependence on $n_{\text{Fe}}/n_{\text{H}}$ is expected at very large columns.

The second case corresponds to Compton–thick gas, such as the walls of the hypothetical nuclear torus. This case has recently been calculated by Matt *et al.* (1996, 1997) for a range of metallicities and viewing angles. For a $\Gamma = 1.9$ continuum, larger than solar $n_{\text{Fe}}/n_{\text{H}}$ and $\cos(i) = 0.5$, where i is the angle between the line of sight and the axis of the torus, Matt *et al.* estimate (see their Fig. 2),

$$\text{EW}(6.4 \text{ keV}) \simeq 1.8(1 + 0.6 \log[\frac{n_{\text{Fe}}/n_{\text{H}}}{4 \times 10^{-5}}]) \text{ keV}. \quad (2)$$

The range of observed angles can change this value by up to a factor of 1.5. Thus, for a typical $\Gamma = 1.9$ continuum, the Compton–thin and Compton–thick assumptions result in a factor 2 difference in the estimated iron abundance. The two cases also predict very different 6–10 keV continuum shape since the Compton–thick gas produces a much stronger 7.1 keV absorption edge. Finally, in Compton–thick gas, some 10% of the 6.4 keV line intensity is in a broad red wing. Below we discuss the iron abundance under the two different scenarios. While the emphasis is on line intensities, we note that our continuum fits do not require the presence of a 7.1 keV absorption in any source except NGC 6240.

The following examples consider two gas components, one represents “cold” (small U_x) gas and the other “hot” (large U_x) gas. Each scatters the central radiation and produces a scattered continuum. We refer to these as the “two continuum components”. We first assume both components to be Compton–thin. In estimating the iron abundance from the observed EW, we note that the two continuum components are contributing at 6.4 keV and Γ is not directly measurable since scattering affects the observed continuum shape (§2.2). We use the numerical calculations (Fig. 2) and assumed that the iron composition

is identical in all components. We also note that resonance absorption is negligible, because iron is in a very low ionization state in the cold component and the column density is large in the hot component. Given these assumptions, we expect each component (hot or cold) to have a similar $\text{EW}(\text{Fe K}\alpha)$ *relative to its own continuum*. Thus, in those sources where the 6.7–6.96 keV iron lines are much weaker than the neutral 6.4 keV lines, most of the 6.4 keV continuum is due to reflection by the neutral component. Given the assumed continuum shape, this implies an iron over abundance by a factor 2–3 for Circinus and a factor of 1–1.5 for Mkn 3. For NGC 6240 and NGC 4388, we estimate the EW relative to the scattered component by using our best fit model of these source (Fig. 6). According to the model, about half the observed 6.4 keV continuum is due to transmission and the other half due to scattering. We can thus estimate $\text{EW}(6.4 \text{ keV})$ relative to the scattered component and deduce $n_{\text{Fe}}/n_{\text{H}} \simeq 1.5 - 2 \times \text{solar}$. Mkn 348 is so different in this respect that we cannot reliably estimate $\text{EW}(\text{Fe K}\alpha)$ relative to the scattered continuum. The iron abundance in NGC 1068, assuming a Compton-thin gas, has been discussed by Marshall *et al.* (1993) and Netzer & Turner (1997), and found to be about three times solar. Thus, under the Compton-thin assumption, we have indications of iron overabundance in 5 sources.

Regarding the Compton-thick case, the iron abundance inferred from the observed $\text{EW}(\text{K}\alpha 6.4 \text{ keV})$ line is about half the value deduced above, i.e. consistent with solar for all sources. As we show below, the analysis of the highly ionized gas enables an independent check on the iron composition because the medium producing such lines is unlikely to be Compton-thick.

4.2. Diagnostic diagrams

Diagnostic diagrams, involving various line ratios, have been used to separate Seyfert galaxies from galactic HII regions, and to search for the spectroscopic signature of LINERs (e.g. Baldwin, Phillips & Terlavich, 1981). Below we attempt to use the same method in the X-ray domain, in search for the unique signature of scattering-dominated AGN.

There are two major differences between our study and the investigation of the optical spectrum of LINERs and HII regions. First, the number of available X-ray lines is very small and we can only measure, reliably, three line ratios and construct two such diagrams. Second, given the gas is photoionized, the X-ray line spectrum is dominated by recombination and not a single, purely collisionally excited line is strong enough to be used. Collisionally excited X-ray lines dominate the spectrum of hot plasmas with ratios vastly different from that expected in photoionized gas. Thus, there is no overlap in properties and line ratio diagrams can either be used for photoionized gas or for hot plasmas. In contrast,

lower excitation photoionized nebulae contain a mixture of recombination and collisionally excited lines that provide very useful diagnostics. Thus ratios like $[\text{O III}] \lambda 5007/\text{H}\beta$ have been used to derive the level of ionization of the gas and line ratios involving highly excited O^{+2} transitions have been used to investigate the role of shock excited gas in the spectrum of LINERs and Seyfert galaxies (e.g. Ferland and Netzer 1983). This kind of analysis is not yet possible in the X-ray regime.

Fig. 7 shows a diagnostic diagram composed of the best observed line ratios in our sample, $I(\text{Si XIII } 1.85 \text{ keV})/I(\text{Fe XXV } 6.7 \text{ keV} + \text{Fe XXVI } 6.96 \text{ keV})$ versus $I(\text{Mg XI } 1.34 \text{ keV})/I(\text{Si XIII } 1.85 \text{ keV})$. The first ratio is a good indicator of regions of large ionization parameters, with electron temperature of the order of 10^6 K, and the second measures the conditions in lower ionization gas. Obviously, the excitation and ionization of Mg XI 1.34 keV and Si XIII 1.85 keV is rather similar and future analysis, based on oxygen and neon lines, will be of greater use. Measurements of the two ratios are available for Circinus and NGC 1068 and an upper limit can be obtained for Mrk 3 (see §2). The diagram shows the location of the three objects along with four theoretical curves, this time assuming the $L_E \propto E^{-0.5}$ continuum. Similar results, with appropriate scaling of U_X , are obtained for the $L_E \propto E^{-0.9}$ continuum used in most other calculation. The curves are series of increasing U_X for various column density and gas composition. The solid lines are standard composition models for three column densities, $N_{\text{H}}=10^{22.4} \text{ cm}^{-2}$, 10^{23} cm^{-2} and $10^{23.3} \text{ cm}^{-2}$. The dotted line is for $N_{\text{H}}=10^{23} \text{ cm}^{-2}$ but with $n_{\text{Fe}}/n_{\text{H}}$ three times larger.

Inspection of the line ratio diagram, and the observed spectra, suggest that:

1. The observed line ratios cannot be simultaneously obtained in a single temperature collisionally ionized gas. Under such conditions, the temperature required to ionize FeXXV and FeXXVI is inconsistent with the observed strength of the silicon and magnesium lines. If all lines are produced in a single component, this gas must be photoionized. Indeed, *ASCA* spectra of starburst galaxies (e.g. Ptak *et al.*, 1997) generally show strong silicon and sulphur lines but little or no emission from neutral Fe $K\alpha$.
2. The inferred ionization parameter, $U_X \sim 1$, is 3–10 times larger than the ionization parameter of the highly ionized (warm absorber) gas in Seyfert 1 galaxies (George *et al.*, 1998). This is in agreement with the finding of Turner *et al.* (1997a). We have examined the properties of this gas and found a mean electron temperature of about 10^6 K and no noticeable soft absorption features. Such gas, on the line of sight to a typical AGN continuum, with a column density not exceeding 10^{23} cm^{-2} (the column density of the great majority of warm absorbers in Seyfert 1 galaxies, see George *et al.* 1998) would escape detection by *ASCA* type instruments.

3. The diagnostic diagram cannot, by itself, be used to infer the Fe/Si abundance ratio since large column densities mimic the appearance of a small-column with large Fe/Si. As argued in §4.1, the analysis of the 6.4 keV lines suggest large $n_{\text{Fe}}/n_{\text{H}}$ in all sources if the emitting medium is Compton-thin. If the high ionization components have similar compositions, then according to the diagram, they must have relatively small column densities, perhaps similar to the lowest column shown in Fig. 7.
4. The weakness of Mg XII 1.47 keV and Si XIV 2.0 keV lines is somewhat surprising. The lines are predicted to be similar in strength to the lower ionization magnesium and silicon lines (Figs. 2 and 3) yet we could only obtain upper limits. The difficulty of detecting the Si XIV 2.0 keV line may partly be explained by the notorious detector/mirror features in *ASCA* around 2 keV.

4.3. The scatterer location and the value of R_f

So far we have focused on relative line intensities and line-to-continuum flux ratios. These are useful in determining the ionization and composition but do not reveal the reprocessing efficiency, R_f , since $\text{EW}(\text{Fe } 6.4 \text{ keV})$ is almost independent of the column density (Fig. 1). R_f can not be obtained by comparing the absolute line flux with the intrinsic luminosity since the latter is not known. However, there are several other luminosity indicators at longer wavelength, including the infrared flux and the $[\text{O III}] \lambda 5007$ luminosity (e.g. Mulchaey *et al.*, 1994, see extensive discussion in Turner *et al.*, 1997b,1998), that can be used. Here we chose to use the reddening-corrected narrow $\text{H}\beta$ line as our luminosity indicator. This is similar to the $L([\text{O III}] \lambda 5007)$ method used in Turner *et al.* but enables a more direct comparison with the intrinsic ultraviolet luminosity.

Measurements of the narrow $\text{H}\beta$ flux for the six sources, as well as for most known type II AGN, are readily available (Mulchaey *et al.*, 1994; Polletta *et al.*, 1996; and references therein). The above references contain also the measured $\text{H}\alpha/\text{H}\beta$ line ratio which we use to correct for reddening and to obtain the intrinsic $\text{H}\beta$ flux. In the following we assume an intrinsic $I(\text{H}\alpha)/I(\text{H}\beta)=3.0$ and a simple galactic type reddening with $A_V/E_{B-V}=3.1$. Reddening corrected $\text{H}\beta$ fluxes obtained this way are listed in Table 1.

A word of caution is in order. Applying a simple, screen-type reddening correction to the spectrum of Circinus and NGC 6240 is problematic since the observed Balmer decrement in both galaxies is very large (e.g. Fosbury and Wall 1979 for the case of NGC 6240). In addition, much of the $\text{H}\beta$ flux in NGC 6240 is likely due to luminous star-forming regions in this galaxy. In both cases, and probably in many other narrow-line galaxies showing

large Balmer decrements, the geometry is rather complex with several clouds along each line-of-sight. We may be looking into dusty environments for which a simple correction factor is inappropriate. This can invalidate the reddening-corrected $H\beta$ fluxes used here.

The theoretical $I(\text{Fe K}\alpha)/I(H\beta)$ is easily obtained from the spectral energy distribution, the column density and the iron abundance. For low ionization, small Balmer optical depth gas, the number of $H\beta$ photons is a known fraction (about 0.12 for Case B recombination) of the Lyman continuum photon flux and the number of $\text{Fe K}\alpha$ photons is a known fraction of the ionizing $E > 7.1$ keV flux. The case of interest for this study is gas with very large Lyman optical depth yet relatively small hard X-ray optical depth. Defining $Q_{7.1 \text{ keV}}$ as the photon flux above 7.1 keV, and $Q_{13.6 \text{ eV}}$ as the Lyman continuum photon flux, we get for this case

$$I(\text{FeK}\alpha)/I(H\beta) \simeq 1.5 \times 10^3 \exp(-\tau_{6.4\text{keV}}) \left[\frac{Q_{7.1 \text{ keV}}}{Q_{13.6 \text{ eV}}} \right] [1 - \exp(-\tau_{7.1\text{keV}})] , \quad (3)$$

where

$$\tau_{7.1\text{keV}} \simeq 0.13 \left[\frac{N_{\text{col}}}{10^{23}} \right] \frac{(n_{\text{Fe}}/n_{\text{H}})}{4 \times 10^{-5}} , \quad (4)$$

is the 7.1 keV optical depth due to iron (assumed to be much smaller than unity), and $\tau_{6.4\text{keV}}$ is the absorption optical depth due to all metals, at 6.4 keV (of the same order as $\tau_{7.1\text{keV}}$ for solar $n_{\text{Fe}}/n_{\text{H}}$). Thus at small $\tau_{7.1\text{keV}}$, the line ratio increases with the iron abundance. Major complications arise due to absorption of the $E > 7.1$ keV photons by elements other than iron and by the non-negligible opacity at 6.4 keV, resulting in the destruction of emitted $\text{K}\alpha$ photons. This makes the $\text{Fe K}\alpha$ emissivity sensitive to the covering fraction since the $\text{K}\alpha$ photons emitted by one cloud can be absorbed by another cloud. Having in mind the NLR conditions, we assume in the following $C_f=0.1$.

Fig. 8 shows a series of calculated $I(\text{Fe K}\alpha)/I(H\beta)$ for $N_{\text{E}} \propto E^{-1.9}$ continuum, solar metallicity, $n_{\text{H}}=10^4 \text{cm}^{-3}$ applicable to the NLR, and various α_{ox} . To enable a comparison with the expressions given above, we note that for those models with $\alpha_{ox}=1.3$, $Q_{0.1-10 \text{ keV}}/Q_{7.1 \text{ keV}} = 130$ and $Q_{13.6 \text{ eV}}/Q_{0.1-10 \text{ keV}} = 52$.

The diagram shows that for $U_x = 10^{-3}$ and $N_{\text{H}} > 10^{21.7} \text{cm}^{-2}$, $H\beta$ is already emitted at maximum efficiency while the $\text{Fe K}\alpha$ flux is proportional to the column density. For $N_{\text{H}} > 10^{23.5} \text{cm}^{-2}$, both lines are emitted at maximum efficiency and their ratio reflects the spectral energy distribution, $n_{\text{Fe}}/n_{\text{H}}$ and the destruction of the $\text{Fe K}\alpha$ photons.

Inspection of Fig. 8 and Table 1 suggests that in four sources, NGC 1068, NGC 6240 Mrk 3 and Mkn 348, the $I(\text{Ka})/I(H\beta)$ line ratio is below 0.2, which is consistent with solar $n_{\text{Fe}}/n_{\text{H}}$ for $N_{\text{H}} < 10^{23.5} \text{cm}^{-2}$ for $\alpha_{ox}=1.1$. Assuming an iron overabundance by 2–3 reduces the required column to below 10^{23}cm^{-2} for the same α_{ox} . Furthermore, in three of the four

cases the required column can be substantially smaller than the above mentioned upper limit. The column density is smaller if the UV bump is weaker than assumed and larger if α_{ox} is larger than assumed. Thus in about half the sources the 6.4 keV iron line could originate in the NLR if the clouds in that region have column densities exceeding about $10^{22.5}$ cm⁻². Circinus and NGC 4388 are different since $I(\text{Fe K}\alpha)/I(\text{H}\beta)$ in those sources is an order of magnitude larger than in the other three. As shown in the diagram, this is unlikely to be due to a much larger column density. Either the X-ray source is very bright compared with the UV source (very small α_{ox}) or else there is an additional, large covering fraction, $\text{K}\alpha$ producing component which is neutral, very thick and inefficient $\text{H}\beta$ emitter.

Current NLR models (see Ferguson *et al.* 1997 and references therein) do not make definite predictions regarding the size of the NLR clouds, since most observed narrow lines originate in the highly ionized, HII part of the clouds. An obvious complication is if the NLR gas is dusty (see Netzer and Laor 1993 and references therein). For example, it is conceivable that the NLR clouds are the illuminated faces of dusty molecular clouds of significant column density. This would result in a reduced $\text{H}\beta$ emissivity but the $\text{Fe K}\alpha$ line will hardly be affected. As already explained, the reddening correction for a dusty HII region can differ substantially from the correction procedure applied here.

We have examined the much larger sample in Turner *et al.* (1997a) to estimate the intrinsic $I(\text{Fe K}\alpha)/I(\text{H}\beta)$ ratio in type II AGN. Out of 17 sources with reliable $\text{Fe K}\alpha$ and $\text{H}\beta$ measurements (including the ones in this paper), 7 show reddening corrected $I(\text{Fe K}\alpha)/I(\text{H}\beta) < 0.2$ which we consider consistent with origin in the NLR of these galaxies. The remaining sources show a larger ratio that requires R_f in excess of what is expected from the NLR gas. The neutral $\text{Fe K}\alpha$ line in those is likely due to absorption by a larger column density, very neutral material that is either the walls of the central torus or large molecular clouds in the nucleus.

Given the likely origin of the 6.4 keV line, we can now comment on the nature and location of the gas producing the high ionization iron lines. Assuming the same $n_{\text{Fe}}/n_{\text{H}}$ in both components, we can derive $R_f(\text{hot})/R_f(\text{cold})$. This is found to be about 1 for NGC 1068 and about 0.1 for Mkn 3 and Circinus. The uncertainty is about a factor 2 since, as explained, the scattering efficiency differs by about this factor when comparing Compton-thin and Compton-thick gas. We further consider possible combinations of covering factor and note that for Compton-thin gas, $R_f \propto N_{\text{H}} \times C_f$. This, combined with $U_x(\text{cold})/U_x(\text{hot})$ (about 10^{-3} with a large uncertainty, see Fig. 1 and the parameters used earlier for the NLR gas), enables us to estimate several likely combinations of these quantities.

An interesting possibility involving the NLR idea, is that $N_{\text{H}}(\text{hot}) \sim 10^{-2} N_{\text{H}}(\text{cold})$.

This would imply $C_f(\text{hot}) \simeq 10C_f(\text{cold})$, i.e. $C_f(\text{hot}) \simeq 1$. In this case, the hot and cold components coexist, spatially, and the large $C_f(\text{hot})$ does not allow a torus with a small opening angle. The typical NLR density is about 10^4 cm^{-3} , thus $n_H(\text{hot}) \sim 10 \text{ cm}^{-3}$. The physical thickness of the hot gas in this case is of order 10-100 pc, i.e. of the same order of the NLR size. We note, however, that the two components are not in pressure equilibrium since $nkT_e(\text{cold}) \simeq 10nkT_e(\text{hot})$. Another possibility is that $C_f \sim 0.1$ in both components and $N_H(\text{cold}) \simeq 10N_H(\text{hot})$. This does not allow a co-spatial existence of the two components. Finally, the 6.4 keV line may be from the thick torus walls. The efficiency in this case is very large and suggests that the fraction of this wall visible to us is extremely small. It also suggests that the hot gas completely fills the opening in the torus.

Acknowledgments: It is a pleasure to acknowledge stimulating and useful discussions with our colleagues R. Mushotzky, K. Nandra, T. Yaqoob and T. Kallman. A very useful referee report helped us improve the presentation of this paper. This research is supported by the Universities Space Research Association (TJT, IMG) and by a special grant from the Israel Science Foundation (HN).

REFERENCES

- Antonucci, R., 1993, ARA&A, 31, 473
- Baldwin, J.A., Phillips, M.M., & Terlevich, R., 1981, PASP, 93, 5
- Burke, B.E., Mountain, R.W., Daniels, P.J., & Dolat, V.S., 1994, IEEE Trans.Nuc.Sci., 41, 375
- Ferguson, J.W., Korista, K.T., Baldwin, J.A., & Ferland, G.J., 1997, ApJ, 487, 122
- Ferland, G.J., & Netzer, H., 1983, ApJ 264, 105
- Fosbury, R.A.E., & Wall, J.V., 1979, MNRAS, 189, 79
- George, I.M., & Fabian, A.C., 1991, MNRAS, 249, 352
- George, I, Turner, T.J., Netzer, H., Nandra, K., Mushotzky, R.F., & Yaqoob, T., 1998, ApJS, ApJS, 114, 73
- Ghisellini, G., Haardt, F., & Matt, G., 1994, MNRAS, 267, 743
- Iwasawa, K, Fabian, A.C., & Matt, G., 1997, MNRAS, 289, 443
- Krolik, J.H., & Kallman, T.R., 1987, ApJL 320, L5
- Krolik, J. & Kriss, G., 1995, ApJ, 447, 512
- Leahy, D.A., & Creighton, J., 1993, MNRAS, 263, 314
- Lightman, A.P., & White, T.R., 1988, ApJ 335, 57
- Marshall, F.E., *et al.* 1993, ApJ, 405, 168
- Matt, G, 1994. MNRAS, 267, L17
- Matt, G., Brandt, W.N, & Fabian, A., 1996, MNRAS, 280, 823
- Matt, G., Fabian, A.C., & Reynolds, C.S., 1997, MNRAS, 289, 175
- Mulchaey, J.S., Koratkar, A., Ward, M.J., Wilson, A.S., Whittle, M., Antonucci, R.R.J., Kinney, A.L., & Hurt, T., 1994, ApJ, 436, 586
- Nandra, K., George, I.M., Mushotzky, R.F., Turner, T.J., Yaqoob, T., 1997, ApJ, 476, 70
- Netzer, H, 1993, ApJ, 411, 594

- Netzer, H., 1996, *ApJ*, 473, 781
- Netzer, H., 1997, *Astrophys.Sp.Sci.*, 248, 127
- Netzer, H., & Laor, A., 1993, *ApJL*, 404, L51
- Netzer, H., Turner, T.J., & George, I.M., 1994, *ApJ*, 435, 106
- Netzer, H. & Turner, J., 1997, *ApJ*, 488, 694
- Ohashi, T. *et al.*, 1996, *PASJ*, 48, 211
- Polletta, M., Bassani, L., Malaguti, G., Palumbo, G.G.C., & Caroli, E., 1996, *ApJSupp*, 106, 399
- Ptak, A., Serlemitsos, P., Yaqoob, T., Mushotzky, R.F., & Tsuru, T., 1997, *AJ*, 113, 1286
- Tran, H.D., 1995, *ApJ*, 440, 597
- Turner, T.J., George, I.M., Nandra, K., Mushotzky, R.F., 1997a, *ApJS*, 113, 23
- Turner, T.J., George, I.M., Nandra, K., Mushotzky, R.F., 1997b, *ApJ*, 488, 164
- Turner, T.J., George, I.M., Nandra, K., Mushotzky, R.F., 1998, *ApJ*, 493, 91
- Zycki, P.T., & Czerny, B., 1994, *MNRAS*, 266, 1994
- Zycki, P.T., Krolik, J.H., Zdziarski, A.A., & Kallman, T.K., 1994, *ApJ* 437, 597

Table 1. X-ray Emission Lines

Line ID (Energy) keV	Line Flux 10^{-4} photons/cm ² /s	continuum 10^{-4} photons/cm ² /s/keV	EW Observed (eV)
Circinus			
Mg XI 1.34 keV	0.21 ± 0.08	4.9	43
Mg XII 1.47 keV	< 0.10	4.4	< 23
Si XII–XIII	$0.33^{+0.22}_{-0.08}$	3.4	100
Si XIV 2.0 keV	< 0.10	3.0	< 33
S XIV–XV	0.32 ± 0.11	2.4	133
S XVI 2.62 keV	< 0.06	2.1	< 35
Fe I–XXIV	3.10 ± 0.19	1.5	2067
Fe XXV–XXVI + $K\beta$	0.86 ± 0.05	1.4	614
F($H\beta$)= 3×10^{-12} erg/sec/cm ²			
I($H\alpha$)/I($H\beta$)=19			
NGC 6240			
Mg XI 1.34 keV	< 0.05	1.80	< 28
Mg XII 1.47 keV	< 0.13	1.60	< 81
Si XII–XIII	$0.11^{+0.09}_{-0.04}$	1.0	110
Si XIV 2.0 keV	< 0.02	0.70	< 28
S XIV–XV	< 0.14	0.60	< 233
S XVI 2.62 keV	< 0.05	0.50	< 100
Fe I–XXIV	$2.40^{+1.84}_{-0.76}$	2.65	906
Fe XXV–XXVI + $K\beta$
F($H\beta$) $> 5 \times 10^{-11}$ erg/sec/cm ²			
I($H\alpha$)/I($H\beta$)=63(?)			
Mrk 3			
Mg XI 1.34 keV	< 0.07	1.60	< 44
Mg XII 1.47 keV	< 0.12	1.20	< 100
Si XII–XIII	0.11 ± 0.04	0.64	172
Si XIV 2.0 keV	< 0.01	0.51	< 20
S XIV–XV	$0.07^{+0.07}_{-0.03}$	0.39	179
S XVI 2.62 keV	< 0.04	0.36	< 111
Fe I–XXIV	0.38 ± 0.08	0.40	950
Fe XXV–XXVI + $K\beta$	0.07 ± 0.01	0.38	184
F($H\beta$)= 4×10^{-12} erg/sec/cm ²			
I($H\alpha$)/I($H\beta$)=6.6			

Table 1—Continued

Line ID (Energy) keV	Line Flux 10^{-4} photons/cm ² /s	continuum 10^{-4} photons/cm ² /s/keV	EW Observed (eV)
Mrk 348			
Mg XI 1.34 keV	< 0.02	0.20	< 112
Mg XII 1.47 keV	< 0.01	0.15	< 44
Si XII–XIII	< 0.49	0.10	< 490
Si XIV 2.0 keV	< 0.04	0.01	< 214
S XIV–XV	0.06 ± 0.03	0.10	600
S XVI 2.62 keV	< 0.01	0.02	< 68
Fe I–XXIV	0.14 ± 0.07	1.24	113
Fe XXV–XXVI + K β	0.05 ± 0.05	1.0	48
F(H β)= 8.4×10^{-13} erg/sec/cm ²			
I(H α)/I(H β)=7.4			
NGC 4388			
Mg XI 1.34 keV	< 0.04	1.0	< 40
Mg XII 1.47 keV	< 0.03	0.80	< 38
Si XII–XIII	$0.08^{+0.09}_{-0.04}$	0.50	154
Si XIV 2.0 keV	0.05 ± 0.04	0.35	143
S XIV–XV	$0.10^{+0.08}_{-0.05}$	0.28	321
S XVI 2.62 keV	< 0.04	0.26	< 154
Fe I–XXIV	0.70 ± 0.39	1.10	636
Fe XXV–XXVI + K β	0.06 ± 0.06	0.78	77
F(H β)= 3.6×10^{-13} erg/sec/cm ²			
I(H α)/I(H β)=5.9			

Note. — Line Energy (col. 1) and identification (col. 2). (f) denotes the line energy was within 50 eV of a known line, and thus fixed at that energy. Column 4: The Line width, σ , where this is not given, the line was fixed at a width of 3 eV. Column 5: The observed line equivalent width. The tabulated H β fluxes are reddening corrected, as explained in the text.

Table 2: Emperical continuum fit parameters

Object	Γ_{soft}	Γ_{hard}	$N_{H,gal}$ (cm ⁻²)	L_{2-10}^a	$L(soft)=L(hard)^b$
Circinus	1.84 ± 0.55	-0.17 ± 0.35	3.0×10^{21}	1.3×10^{41}	3.5 keV
NGC 6240 ^c	1.94 ± 0.13	1.94 ± 0.13	5.5×10^{20}	5.2×10^{42}	5.7 keV
Mrk 3	2.90 ± 0.51	0.32 ± 0.35	8.7×10^{20}	2.6×10^{42}	2.6 keV
Mkn 348 ^d	2.77 ± 0.87	1.50 ± 0.30	1.2×10^{20}	4.0×10^{42}	2.2 keV
NGC 4388	3.5 ± 0.5	$-0.62^{+0.65}_{-0.21}$	2.6×10^{20}	2.0×10^{42}	2.8 keV

^aObserved Luminosity in erg s⁻¹, assuming $H_0 = 50$, $q_0 = 0.5$

^bThe energy at which the soft and the hard components contribute equal amounts

^cadditional column of $1.5^{+1.4}_{-0.8} \times 10^{24}$ cm⁻² covering $0.99^{+0.01}_{-0.07}$ of the continuum is included in the model

^dadditional column of 1.41×10^{23} cm⁻² covering the hard component is included in the model

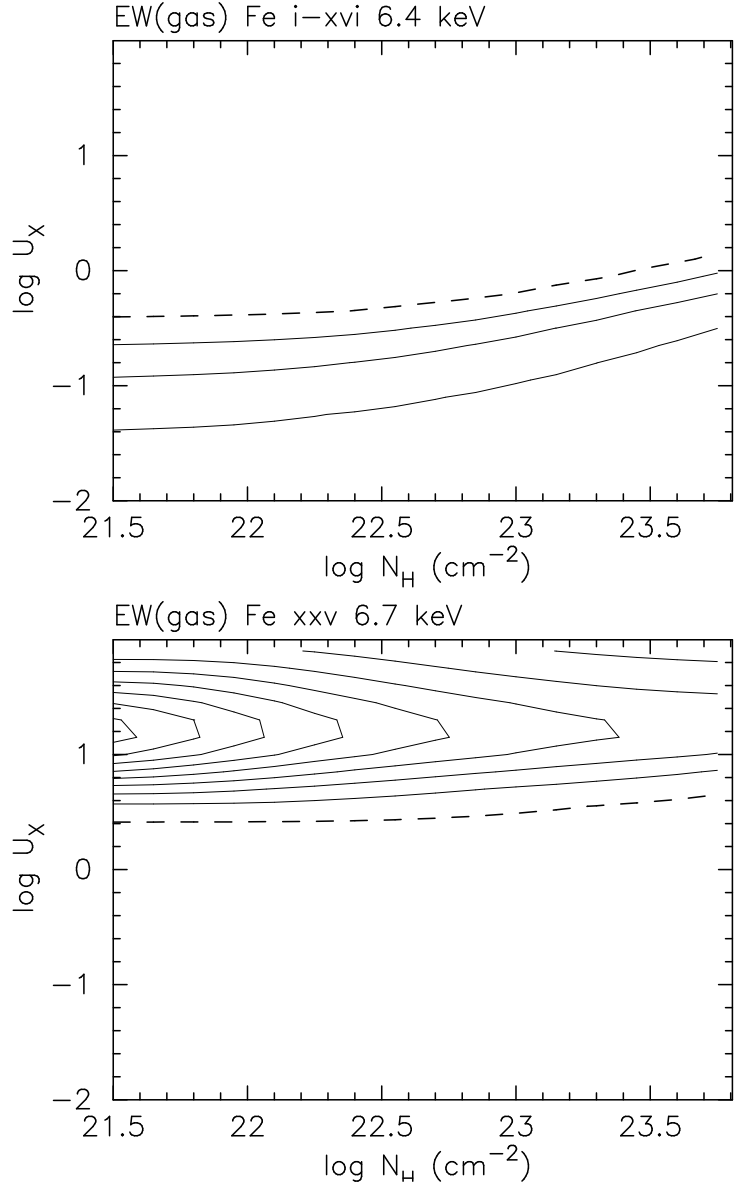


Fig. 1.— Calculated $\text{EW}(\text{Fe K}\alpha)$, relative to the scattered continuum, for “neutral” (FeI–xvi) and He-like iron lines. The 1–50 keV energy slope is 0.9, the covering factor is 0.5, $n_{\text{Fe}}/n_{\text{H}} = 4 \times 10^{-5}$ and the microturbulent velocity equals the local sound speed. The contours are separated by 200 eV, starting at $\text{EW}(\text{Fe K}\alpha)=100$ eV (dashed line). Note the large EW of the Fe xxv 6.7 keV line at small columns due to resonance absorption. The results are insensitive to the exact covering fraction except for $C_f > 0.95$.

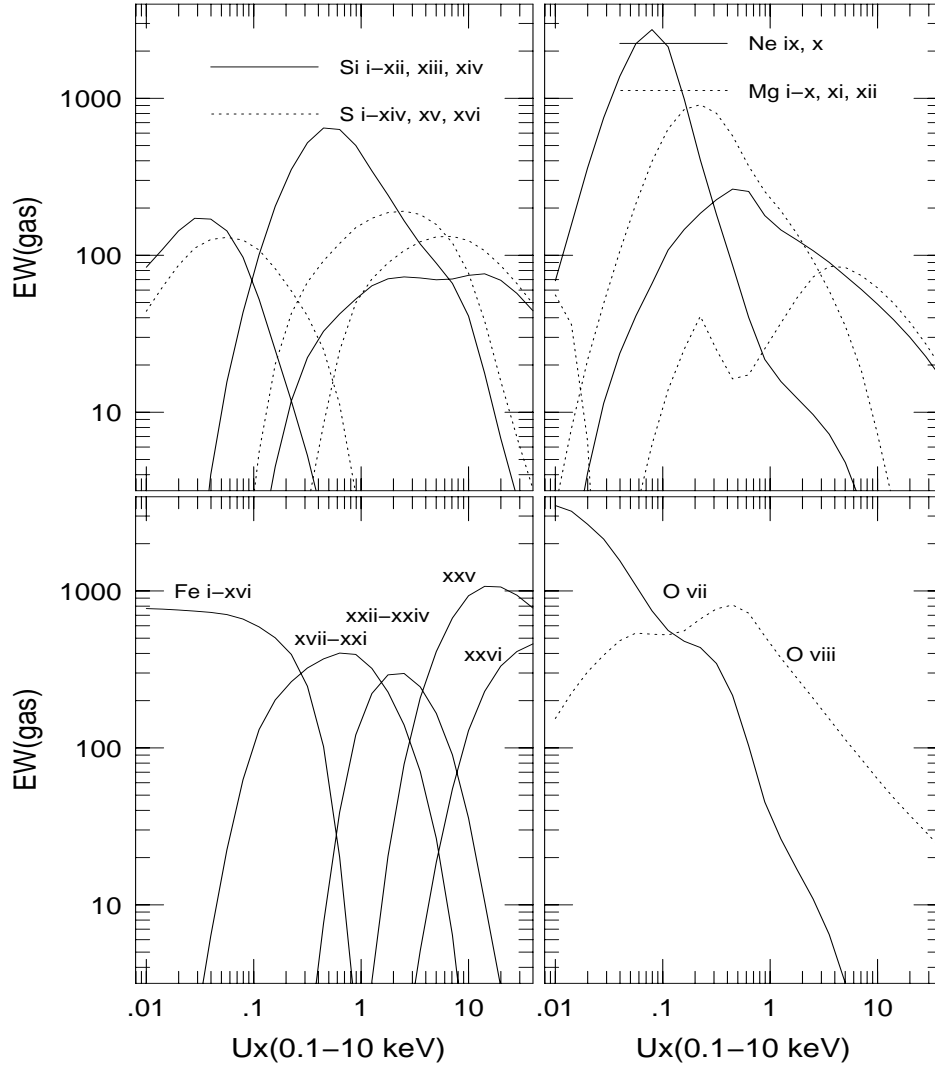


Fig. 2.— Equivalent widths, in eV, relative to the scattered continuum, as a function of ionization parameter. Standard composition gas (see text) with density of 10^8cm^{-3} , column density of $10^{22.4} \text{cm}^{-2}$, $N_E \propto E^{-1.9}$, and covering fraction of 0.5. The top two panels show three lines for each of neon, magnesium, silicon and sulphur; a “neutral” line (i.e. all transitions in ions with three or more electrons), the He-like line and the H-like line. The lines are easily recognized by the increasing level of ionization (from left to right in the diagram).

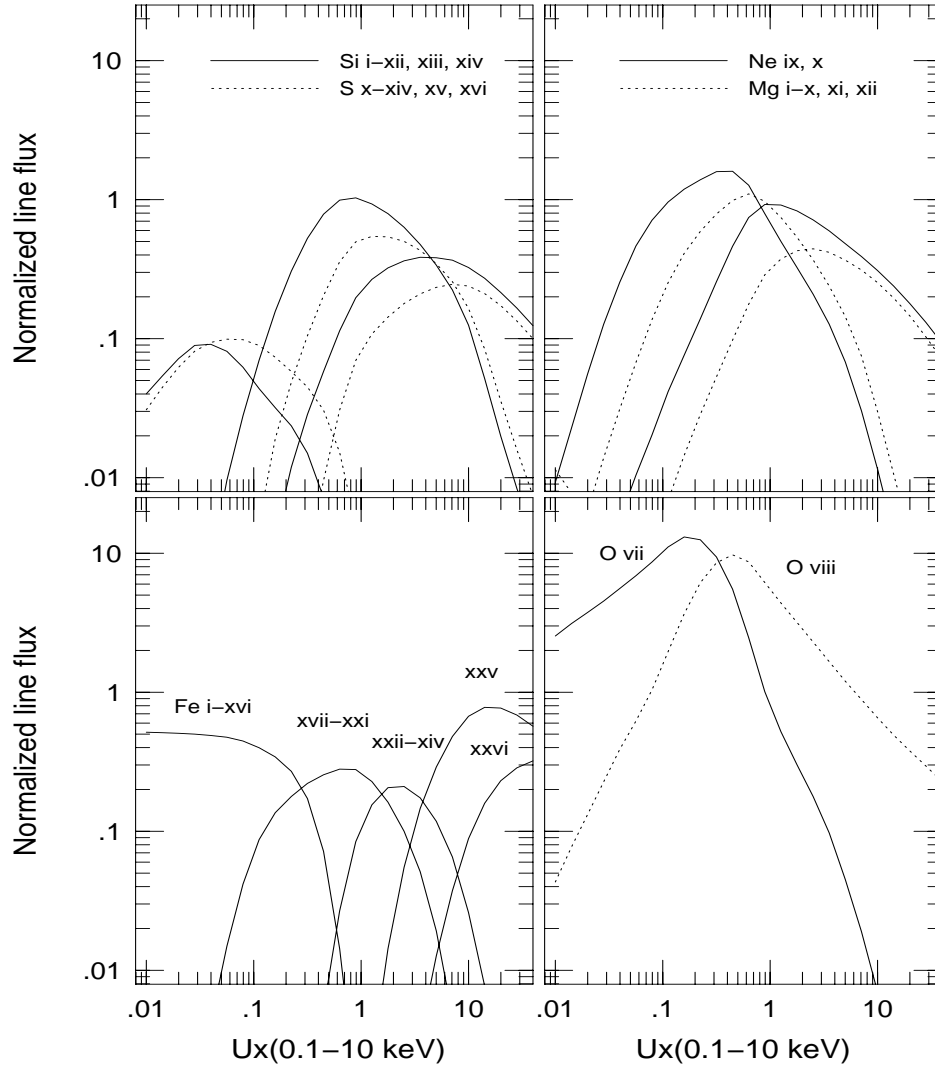


Fig. 3.— As in Fig. 2 except that normalized line intensities, relative to the incident continuum at 0.65 keV, are shown.

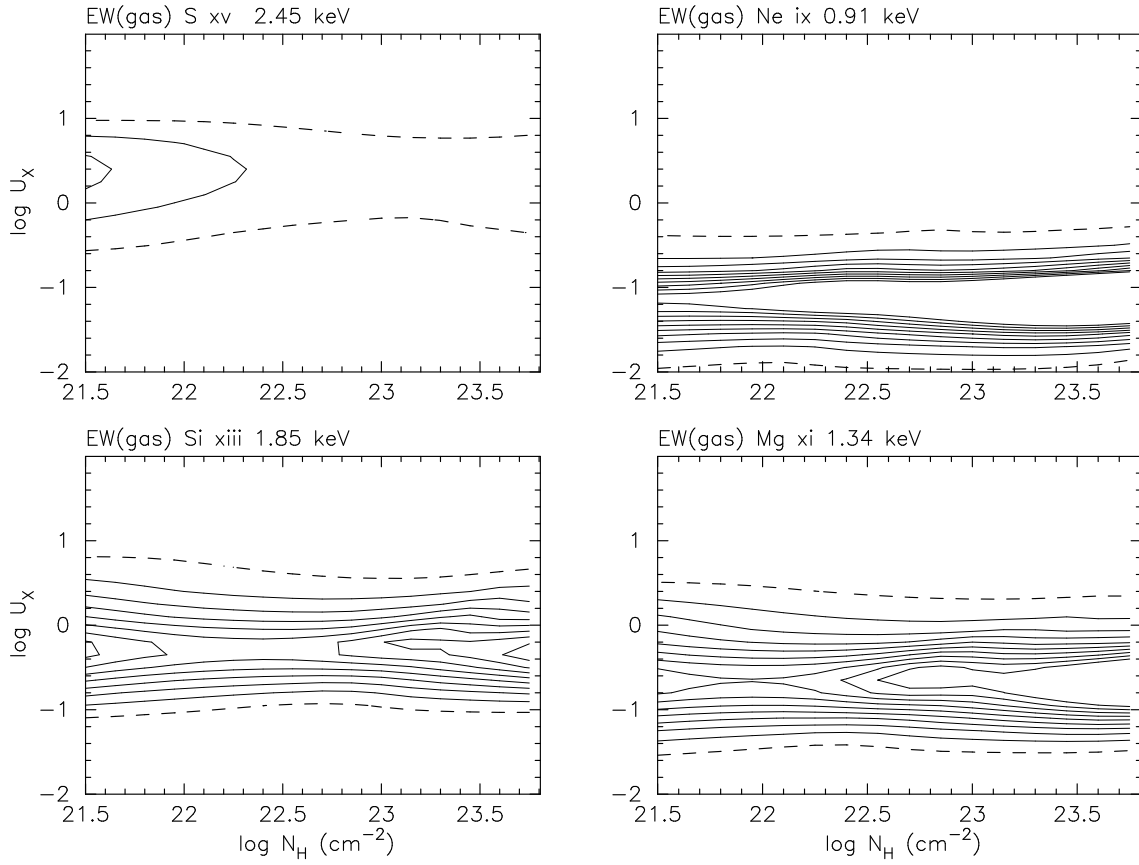


Fig. 4.— Line equivalent widths, relative to the scattered continuum, for various soft X-ray lines. Contours start at $\text{EW}=100$ eV and are separated by 100 eV, except for Ne IX 915 eV where they start at 100 eV but separated by 200 eV. The lowest contour in all cases is plotted with a dashed line.

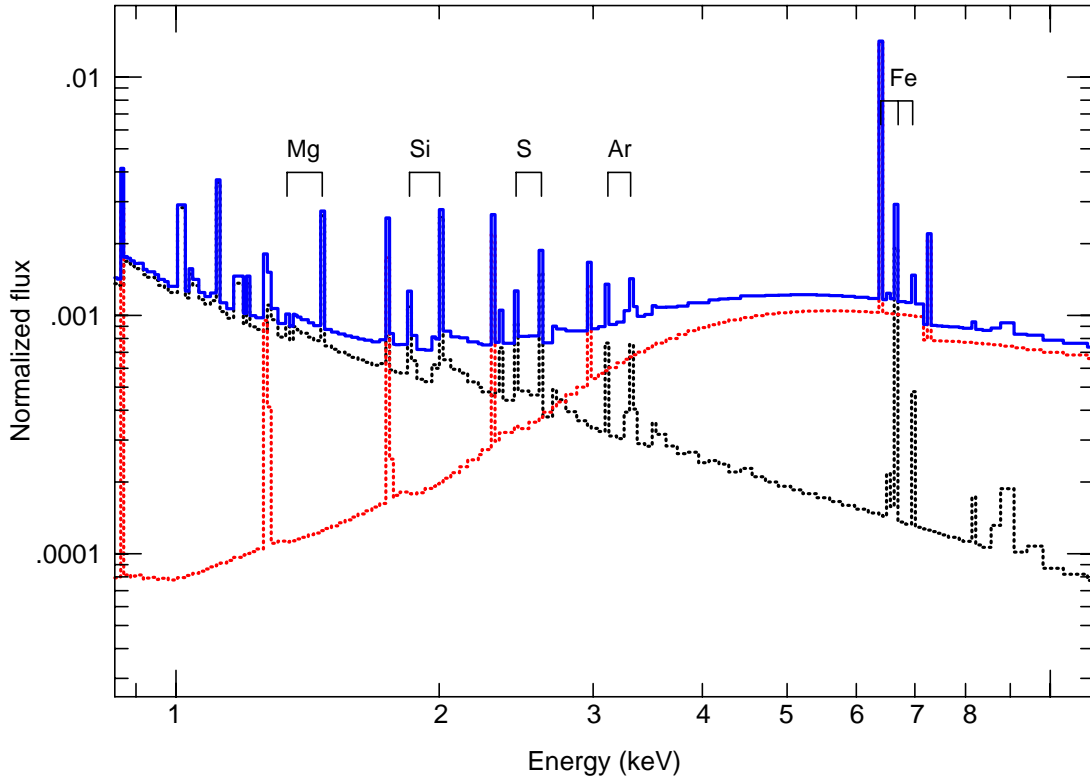


Fig. 5.— Scattered SEDs for an intrinsic $N_E \propto E^{-1.9}$ continuum and two different clouds: one with $N_H=10^{23}\text{cm}^{-2}$ and $U_X=10^{-3}$ (the rising spectrum) and the second with $N_H=10^{22}\text{cm}^{-2}$ and $U_X=10$. The two are normalized to give a ratio of about 10:1 at 6.4 keV, which produces the Fe $K\alpha$ line ratios observed in all cases except for NGC 1068. Note the very flat appearance of the combined (solid line) spectrum).

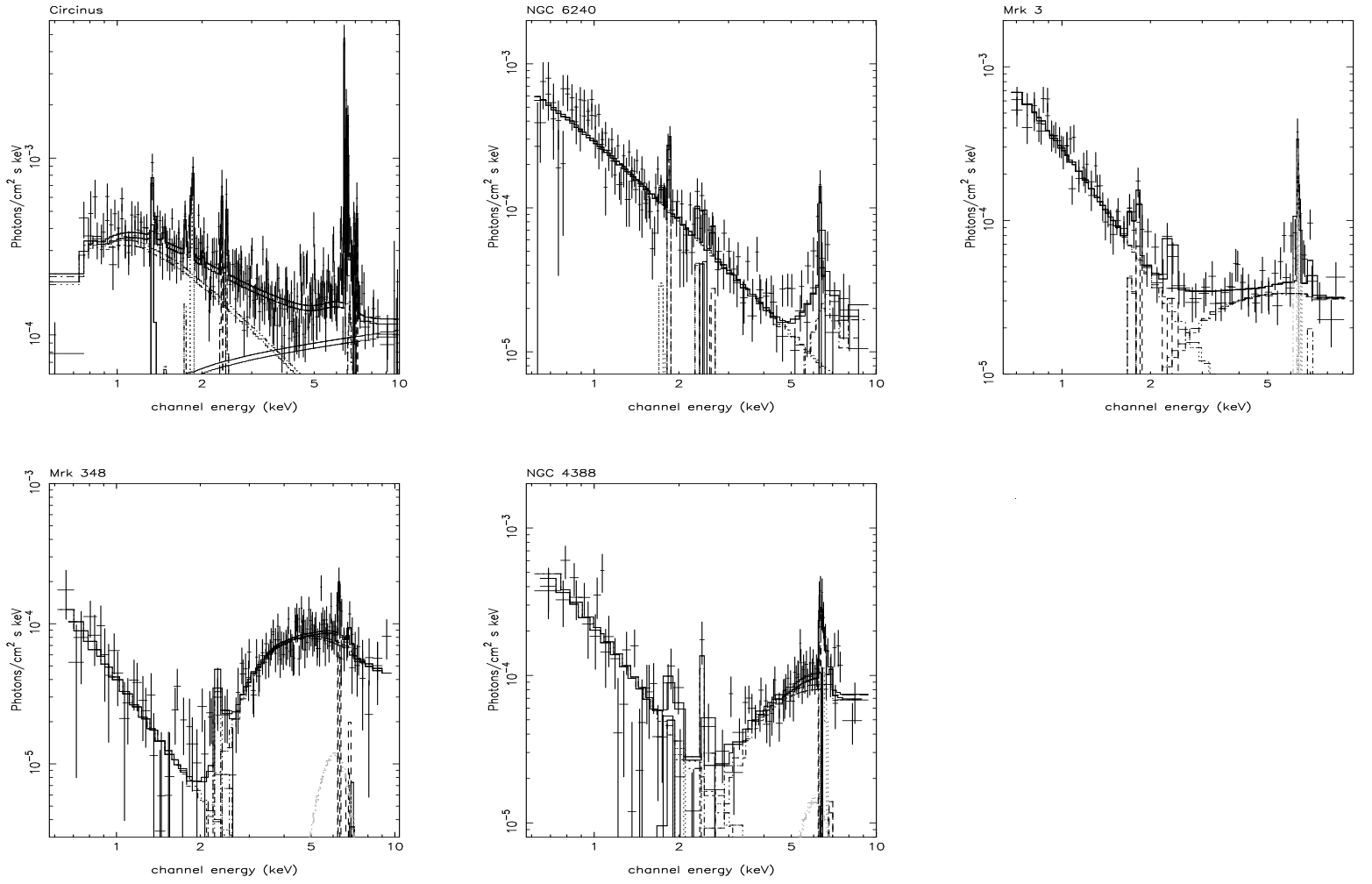


Fig. 6.— SIS data and fitted models for five scattering-dominated AGN.

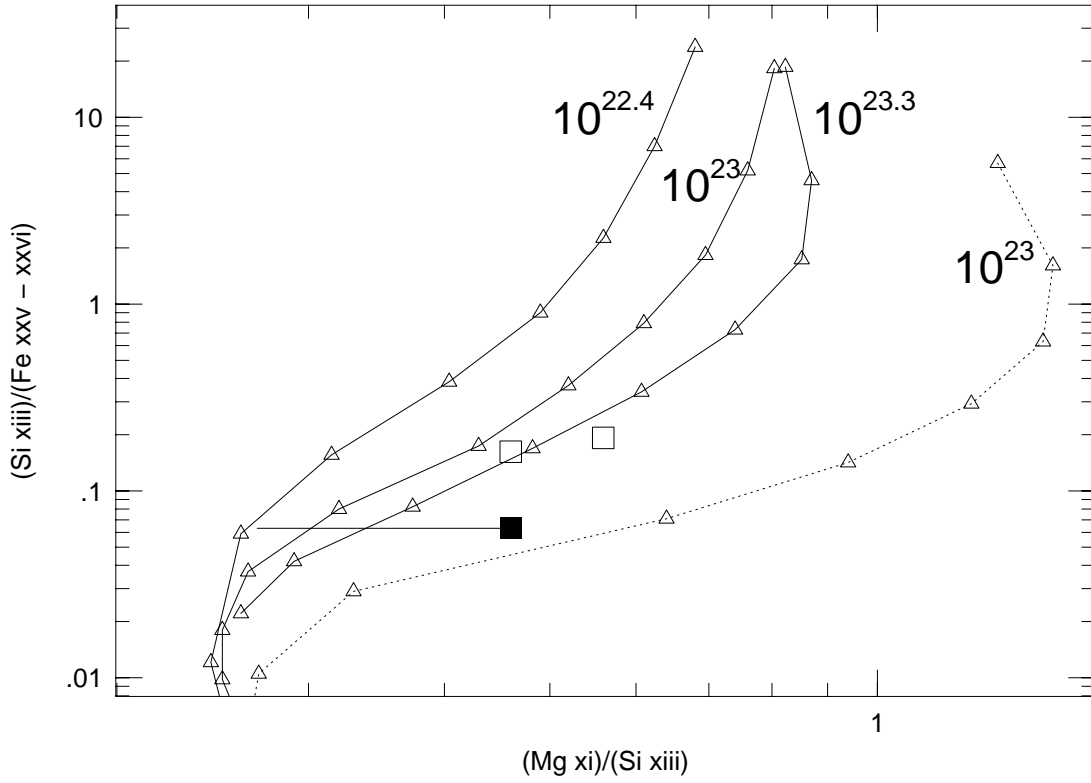


Fig. 7.— A line ratio diagram for three AGN. The curves represent series of increasing ionization parameter for the column density marked. In all curves, $U_{\text{X}}=10^{-0.4}$ at the top and increases downward, by 0.1dex per step. The solid lines are for the assumed standard composition and the dotted line for $n_{\text{Fe}}/n_{\text{H}}$ three times larger and all other abundances not altered.

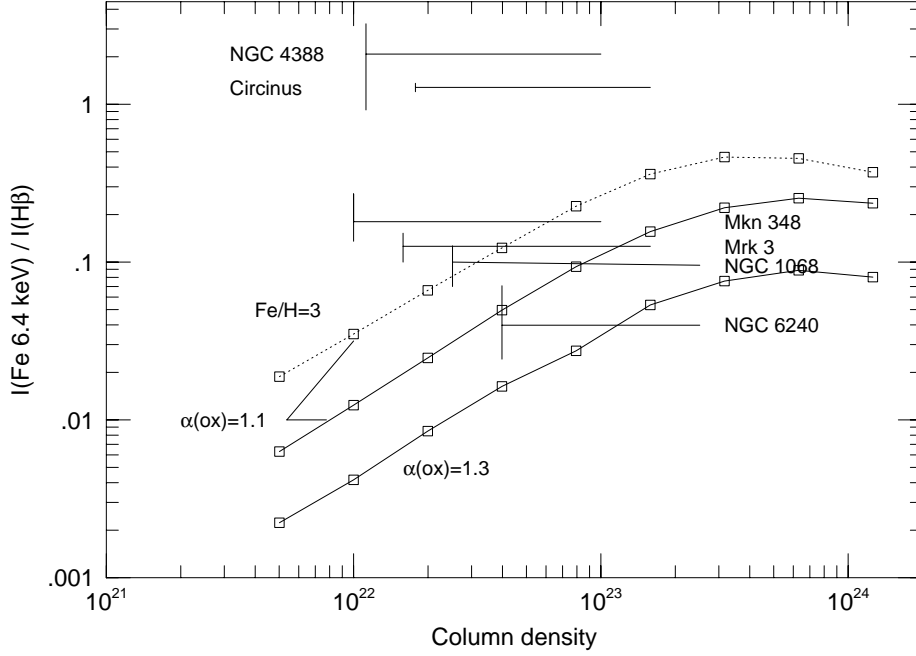


Fig. 8.— Theoretical Fe $K\alpha$ / $H\beta$ as a function of column density for the $L_E \propto E^{-0.9}$ X-ray continuum, $C_f=0.1$, $U_X=10^{-3}$ and various α_{ox} , as marked. The solid lines are for the standard metallicity and the dotted line for n_{Fe}/n_H three times larger. The horizontal lines mark the observed line ratio in our sample. The associated error bars correspond to the uncertainties in the Fe $K\alpha$ fluxes and do not include the uncertain reddening correction factors.